Bubbles, Cavities, and the Long-Ranged Attraction between Hydrophobic Surfaces

John L. Parker*,† and Per M. Claesson

Laboratory for Chemical Surface Science, Department of Chemistry, Physical Chemistry, Royal Institute of Technology, S-100 44 Stockholm, Sweden, and Institute of Surface Chemistry, Box 5607, S-114 86 Stockholm, Sweden

Phil Attard

Department of Physics, The Faculties, The Australian National University, Canberra, ACT 0200 Australia

Received: January 21, 1994; In Final Form: May 26, 1994®

Measurements of the forces in water between neutral hydrophobic surfaces prepared by covalent modification of glass are presented. The surfaces are stable under a variety of conditions including high temperature, high salt concentrations and with added ethanol. The forces between these surfaces have been studied under all of these different conditions. In water the force is attractive at very large surface separations, and discontinuities or steps are present in the force curves. It is suggested that the steps at the onset of the force are due to the bridging of submicroscopic bubbles or cavities between the surfaces and that it is their consequent growth with decreasing separation that causes the long-range attraction between hydrophobic surfaces. Electrolyte has a negligible effect on the range and strength of the measured forces, except at very high salt concentrations where the strength of the attractive forces and the adhesion between the surfaces increases slightly. The addition of ethanol reduces both the strength of the long range forces and the adhesion between the surfaces. On the basis of the comparison between these results and earlier measurements, it appears that the attraction does not obey the Derjaguin approximation. Forces were also measured in the presence of a microscopic vapor cavity created by first bringing the surfaces into contact.

Introduction

Direct measurements of the interactions between macroscopic hydrophobic surfaces have revealed the presence of strong attractions of much longer range than the classical van der Waals force.[1-14] The force is in some cases measurable at separations greater than 100 nm. The existence of an interaction at such distances challenges fundamental notions of liquid structure and surface forces, and despite considerable theoretical effort the molecular origin of this long-range attraction remains controversial.

A number of explanations of the range and the strength of the interaction have been proposed. It has been shown that the force might originate from a perturbation in the ordering of water propagating through the liquid between two hydrophobic surfaces,[15] a hypothesis that is difficult to test by experimental or by numerical simulation. Other ideas invoke an electrostatic interaction to account for the range, and various origins for the strength of the attraction. The latter include (i) correlated fluctuations of polarization due to the state of the water adjacent to the hydrophobic surface,[16] (ii) an instability in the electrolyte between the surfaces,[17] and (iii) electric fields associated with large ordered crystalline domains in the adsorbed surfactant films.[14] These electrostatic theories predict that the range of the interaction should scale with the Debye length of the electrolyte. However, this salt dependence is not observed.[9] It has also been suggested that fluctuations in the water interface at the hydrophobic surface correlate hydrodynamically to produce an attractive force.[18] A final theory, focusing on the observed cavitation of the water when the hydrophobic surfaces are separated from contact,[5] postulates the existence of a separation-induced spinodal[19] and invokes the long-range attractions that occur in a metastable bulk fluid near the spinodal line.[20]

The theory of Bérard et al.[19] invokes a metastable liquid beyond liquid-vapor coexistence. Vapor is observed between the surfaces after they are brought into contact,[5] and the force in the presence of visible microscopic vapor cavities has been calculated.[21,22] Liquid and vapor can coexist between the surfaces at surprisingly large separations, as can be seen by applying an equation for capillary condensation in slit pores.[23-25] The pressure drop $\Delta p = p_v - p_l$ is for sufficiently large cavities related to the surface tension and the radius of curvature of the straight liquid-vapor interface connecting two flat surfaces by the Laplace-Young equation, $\Delta p = -\gamma_{lv}/r$, and by simple geometry this radius is related to the contact angle by $r = -H_0/(2\cos\theta)$. This gives the coexistence separation

$$H_0 = 2\gamma_{lv}\cos\theta/\Delta p \qquad (1)$$

For water one has $\gamma_{lv} = 0.072 N/m$, $\Delta p \approx -10^5 N/m^2$, and for certain hydrophobic surfaces, $\theta = 110°$. These give a coexistence separation of 0.5 μm. If the pressure drop is smaller, the coexistence separation, of course, becomes larger.

The force measurements are performed at smaller separations than this, and vapor is not visible prior to contact. If no cavitation occurs and the interlayer remains a liquid, then according to this equation it is metastable, and the theory of Bérard, et al.[19] may well be applicable. If one the other hand vaporization does occur, then any bubbles or cavities must be of submicroscopic size in order to remain invisible. The questions then become whether such submicroscopic cavities are stable, whether they can occur prior to contact, and whether they can give rise to the measured forces.

In this paper we present experimental and theoretical evidence which supports the latter view. High-resolution force measurements show discontinuities or steps at the large-separation onset of the attraction. We interpret these jumps in force as signifying the appearance of vapor/gas bridges between the surfaces. Separation-induced spinodal attractions[19] are inconsistent with the present experiments since that theory applies *prior* to a first-order transition, whereas the force discontinuities found here indicate that the attraction between hydrophobic surfaces occurs

† On leave from the Department of Applied Mathematics, Research School of Physical Sciences, G.P.O. Box 4, Canberra ACT 2601, Australia.

® Abstract published in *Advance ACS Abstracts,* August 1, 1994.

0022-3654/94/2098-8468$04.50/0

after a transition. The force data obtained here are almost independent of electrolyte up to a concentraiton of 5 M. This is contrary to the predictions of theories that invoke an electrostatic origin for the force.[14,16,17] Measurements of the interaction in the presence of divalent electrolytes[9] also indicate that the force has a nonelectrostatic origin. It is concluded that the long-ranged attraction between hydrophobic surfaces most likely originates from submicroscopic bridging bubbles or cavities.

Materials and Methods

A. Surface Force Measurements. Surface forces were measured with a new type of surface force apparatus which has been used in only a few previous studies.[26-28] This apparatus can be operated without interferometric measurements of the surface separation. One surface is mounted at the end of a bimorph force sensor, and the other is mounted at the end of a piezo electric tube. The force sensor is enclosed in a Teflon sheath mounted inside a small stainless steal measuring chamber (volume ~10 mL). The chamber is clamped to a translation stage which is used to control the coarse position of the piezo electric tube and the upper surface. A complete description of the apparatus and its applications will be given in a forthcoming publication.[29]

Measurements are carried out by moving the surfaces toward each other by continuously expanding a piezo electric tube. The voltage applied to expand the piezo actuator is controlled by a computer which also records the response from the bimorph force sensor. When the surfaces have come into adhesive contact, they deform due to elastic compression. A further motion of the piezo tube is transmitted directly to the force sensor, and the signal from the force sensor increases linearly with the expansion of the piezo actuator. Consequently the sensitivity of the bimorph can be calibrated against the known piezo actuator expansion which is independently measured with a linear displacement transducer. In the figures the position of the surfaces after deformation due to the adhesive force is defined as zero separation. The actual contact of the undeformed surfaces thus occurs further out. The effect of the surface deformation on the interpretation of the measured forces is discussed further in the Discussion section. However, it is not possible to define an absolute position of the hard wall with respect to the contact between the surfaces in air. As a result it is not possible to determine the thickness of the hydrophobic layers in situ.

B. Surface Preparation. Extremely smooth glass surfaces can be very simply prepared. These surfaces are also reactive to silanation with chlorosilanes making glass an ideal substrate for surface force measurements. Glass surfaces were prepared by cutting a 3-cm length of a 2-mm-diameter glass rod. The rod was then cleaned with ethanol and the end melted in a gas burner until a molten droplet with a radius of 2 mm was formed.

The bare glass surfaces were rendered hydrophobic by reaction with one of three different types of fluorocarbon silane containing either one, two, or three chlorines bound to silicon. These were (tridecafluoro-1,1,2,2-tetrahydrooctyl)dimethylchlorosilane, (tridecafluoro-1,1,2,2-tetrahydrooctyl)methyldichlorosilane, and (tridecafluoro-1,1,2,2-tetrahydrooctyl)trichlorosilane, henceforth referred to as $FSCl_1$, $FSCl_2$, and $FSCl_3$. The first of these silane reacts with OH groups but does not form polymers, whereas both $FSCl_2$ and $FSCl_3$ can form polymeric species. The silanation techniques used were different for the polymerizable and unpolymerizable silanes. For the polymerizable silanes the surfaces were exposed to the silane vapor for a period of 10 min in a dry desiccator. Heat treatment has been found to be essential in the complete reaction of silanes with silica.[30,31] As a result the surfaces were heated in the absence of silane vapor for a period of 45 min to 1 h at a temperature of 120–150 °C in order to react physisorbed silanes and evaporate any unreacted material.

The monofunctional silane $FSCl_1$ was reacted with glass surfaces at an elevated temperature (120–150 °C) in a sealed vessel. It was found that neutral hydrophobic surfaces could be prepared this way by heating the glass in the presence of the silane vapor. The surfaces were then dried the same way as for the polymerizable silanes.

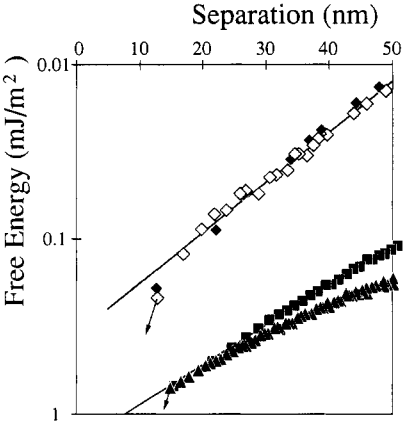

Figure 1. Interaction free energy (E) obtained from the Derjaguin approximation as a function of separation between two hydrophobed glass spheres, $E = F/\pi R$ with $R = 2$ mm, and between hydrophobed mica sheets in the crossed cylinder arrangement, $E = F/2\pi R$ with $R = 20$ mm. The solid squares are results for $FSCl_2$ treated surfaces and the solid triangles $FSCl_3$ treated surfaces. Two separate force curves for mica surfaces coated with a Langmuir Blodgett film of dioctadecyldimethylammonium bromide are also shown (solid and open diamonds). The straight lines are exponential fits to the data $E = Ae^{-D}/\lambda$ with $A = 1.5$ mJ/m^2 and $\lambda = 19$ nm for the $FSCl_2$ results and $A = 0.35$ mJ/m^2 and $\lambda = 15$ nm for the results obtained with hydrophobed mica.

The surfaces obtained in this way expose fluorocarbon chains toward the environment. This renders them strongly hydrophobic with advancing and receding contact angles of 110° and 90°, respectively. Atomic force microscope images of the surfaces show no crystallinity in the films. The maximum variation in height over 400 nm was 0.2 nm.[32] Two surfaces were mounted in the apparatus and aligned with the line connecting the centers of both spheres parallel with the axis of motion of the piezo electric tube. Water was purified with a Millipore UHQ water purification system and deaerated prior to use in the measuring chamber.

Results

A. Surface Force Measurements in Water. The measured force (F) between two spheres of radius of curvature (R) is related to the interaction free energy per unit area (E) between plane parallel plates by the Derjaguin approximation; $F/R = \pi E$. For two crossed cylinders $F/R = 2\pi E$, and with these relationships we can compare the results obtained for two glass spheres with those obtained from the conventional interferometric SFA using crossed mica cylinders. Figure 1 shows the forces scaled by πR from experiments with a pair of $FSCl_2$ coated spheres and a separate pair of $FSCl_3$ treated surfaces. The upper points in Figure 1 are measurements of the attraction between two DODABr (dioctadecyldimethylammonium bromide) coated mica surfaces measured in the interferometric SFA, and these results, which agree quantitatively with previous measurements,[4,5] are scaled by $2\pi R$. These surfaces were prepared with the Langmuir–Blodgett (LB) deposition technique. The interaction free energy between the fluorocarbon surfaces is very much stronger than those measured between surfactant monolayers; nevertheless the exponential attraction has a very similar decay length to the measurements made in the mica system. We argue later that the apparently much stronger interaction between the fluorocarbon surfaces may be due to the inappropriate use of the Derjaguin approximation.

One key difference between the measurements between fluorinated glass surfaces and the LB film measurements is the appearance of steps in the force curves. This is shown clearly in

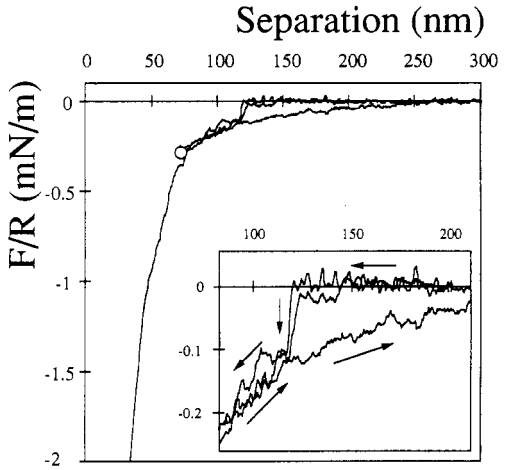

Figure 2. Forces normalized by the radius of curvature (F/R) measured between $FSCl_2$ treated surfaces. The forces were measured both on approach of the surfaces and as they were separated from the point indicated by the circle (expanded in inset); see text for details.

Figure 2, where the forces between $FSCl_2$ in water are shown. There is an abrupt change in force from the zero base line value to ~ -0.1 mN/m, which occurs at a surface separation of ~ 120 nm. The forces for smaller separations than this are exponentially attractive and characteristic of the types of interactions measured between other types of hydrophobic surfaces. Figure 2 also shows the effect of reversing the motion of the surfaces prior to the surface contact. The surfaces were advanced to the point indicated by the circle and then reversed and separated. There is a clear hystersis in the inward and outward going measurements. The separation is usually calculated with respect to the position of the hard-wall contact between the surfaces. Such a hard-wall reference is not measured when the surfaces are reversed prior to contact. In order to obtain the surface separation, the position of the step in force curve was adjusted so that it matched the position of the step in a complete force measurement into contact. The fact that the force as a function of separation after the step (i.e. at smaller separations than the step) agrees perfectly with the measurements on the force run into contact indicates that this procedure is legitimate.

The di- and trifunctional silanes $FSCl_2$ and $FSCl_3$ can polymerize; $FSCl_2$ can form long linear polymers whereas $FSCl_3$ can form three-dimensional polymer networks. There exists then the possibility that the forces between these surfaces are due to bridging polymers, although for $FSCl_2$ this is extremely unlikely because both the backbone and tail of this linear polymer is hydrophobic, and there is no reason that it should dangle out into the aqueous phase. Furthermore, the pull-off force measurements give no indication of anything protruding from the surface. Nevertheless, the possibility that the forces were due to polymer bridging was tested by preparing neutral $FSCl_1$ coated surfaces, and the forces measured between these surfaces are shown in Figure 3. The occurrence of a force discontinuity at large separations is the rule, not an exception, as Figure 3 demonstrates. In fact multiple steps usually occur on any single force run. The separation at which each step occurs is quite variable, but the height of each step is rather regular, which means that several broad bands can be discerned in the data, which are for a single contact position. Qualitatively, at large separations the force directly after any single step is relatively constant, and the force becomes increasingly attractive as more steps occur as the separation is decreased.

When hydrophobized glass surfaces are brought into contact, a vapor cavity forms between them. With the experimental setup used in this study, there is no interferometric measurement of the surface separation, so the formation of the cavity cannot be observed directly. When the surfaces are brought into contact

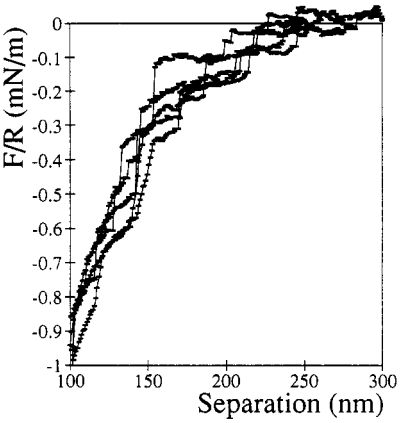

Figure 3. Normalized force on approach of $FSCl_1$ surfaces in water. Each symbol represents a smoothed force-separation datum, (5-point running average, single sided at a step). The lines connecting the data are five separate force runs.

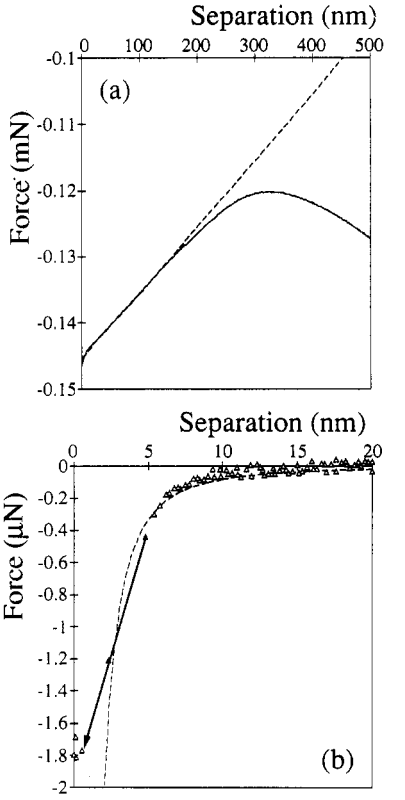

Figure 4. (a) The measured force between 2-mm hydrophobic spheres ($FSCl_2$) in the presence of a microscopic cavity (solid line, arbitrary zero of force). The dashed line is the theoretical force for optimal cavities at each separation ($\Delta p = -1.5 \times 10^4$ N/m^2, and $\gamma_{lv} = 0.072$ N/m, $\theta = 100°$). (b) Short separation attraction with linear cavity term subtracted (symbols) compared to van der Waals attraction between silica in air (dashed line, Hamaker constant 5×10^{-20} J). The arrow denotes the jump into contact.

and then separated to a distance such that water is present between the surfaces (i.e. any cavity which formed in contact has snapped), the force between the surfaces is zero, and as a consequnce the signal from the bimorph is at its base line value. However, the force between the surfaces in the presence of a bridging cavity formed by first bringing the surfaces into contact and then separated them is so attractive and so strong that the signal from the bimorph becomes saturated. As a result, one discharges the bimorph prior to the measurement of the force inside the cavity, so the absolute magnitude of the force is not measured. With the spring constants used in these experiments, it was possible to trap a cavity between the surfaces more often than not; i.e. most often

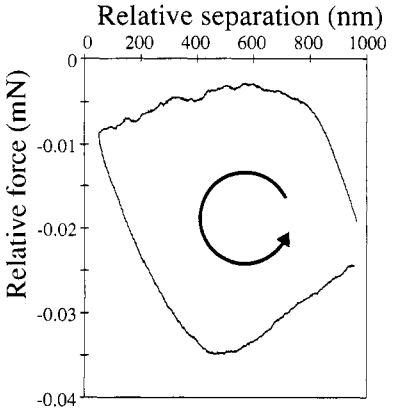

Figure 5. Inward and outward forces measured in the presence of a microscopic cavity (arbitrary zeros).

the surfaces jumped out from adhesive contact, leaving the cavity between the surfaces. Measurement of the force in the presence of the cavity after zeroing the bimorph signal revealed long-range attractive interactions (Figure 4a). The force law measured was distinctly different from that measured with water between the surfaces.

At very small separations in the presence of the cavity, there is a sharp increase in the attraction, which is due to the van der Waals interaction of the solid surfaces across the vapor. This is more evident in Figure 4b, where the linearly varying part of the measurements, which includes the arbitrary zero of force and which corresponds to the cavity contribution, has been subtracted. The van der Waals attraction of silica across air is shown for comparison.[33] The arrow signifies the jump in the data that occurs when the gradient of the force exceeds the spring constant of the measuring bimorph. The force in the presence of a vapor cavity is hysteretic, as Figure 5 shows. The data represent a continuous force measurement; beginning at large separation with a cavity present, the surfaces are first moved toward each other and then apart without coming into contact. In this case only the change in force and change in separation are meaningful, both zeros being arbitrary.

The monofunctional surfaces were prepared by heating method, and a very high coverage of silane is obtained. The adhesion between these surfaces in water is 240 mN/m. The surface energy of the solid contact is γ, which can be obtained from the JKR theory[34] using the relation $F/R = 1.5\pi(\gamma - \gamma_{ss})$, where γ_{ss} is the excess free energy associated with the surfaces in contact. This term is zero for a perfectly smooth molecular contact, and if this term is neglected, the solid–liquid interfacial energy is calculated to be 51 mN/m. Using Young's equation, one obtains a relation between the normalized adhesion force in air to the normalized adhesion force in water, the liquid surface tension and the contact angle:

$$(2F(\text{air})/3\pi R - \gamma_{ss}(\text{air})) - (2F(\text{water})/3\pi R - \gamma_{ss}(\text{water})) = \gamma_{lv}\cos\theta \quad (2)$$

Provided that the excess free energy associated with the surface contact is the same in air and water, eq 2 may be simplified,

$$2F(\text{air})/3\pi R - 2F(\text{water})/3\pi R = \gamma_{lv}\cos\theta \quad (3)$$

This is applicable if the contact between the surfaces is perfectly dry. The advancing and receding contact angle of $FSCl_1$ surfaces is 108 and 90°, respectively. The adhesion of these surfaces in air, 145 mN/m, corresponds to a solid–vapor interfacial energy of 31 mN/m. Using eq 3, the calculated contact angle is 106° which is close to the measured advancing contact angle. If surface deformation effects are ignored one instead obtains $F/R = 2\pi(\gamma - \gamma_{ss})$.[35,36] This gives γ_{sl} = 38 mN/m, γ_{sv} = 23 mN/m, and θ = 102°. We note that the presence of a vapor cavity around the contact zone is not expected to affect the measured adhesion force.[37]

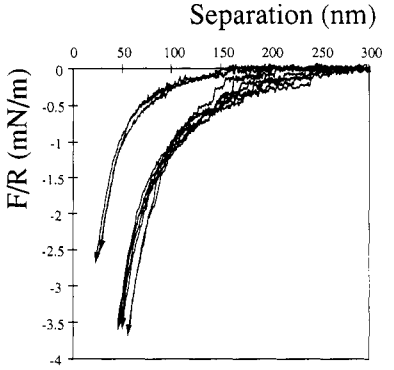

Figure 6. Forces measured between $FSCl_2$ treated surfaces in water in 1 M KBr (two closest curves to the abscissa) and forces between $FSCl_1$ treated surfaces in water and NaCl solutions. The curve in this second group furthest to the left is the result in water and the other curves are 2×10^{-3}, 1×10^{-2}, 0.1, 1, and 5 M, and the strength of the attraction increases with increasing salt concentration.

B. Effect of Electrolyte. We have found that addition of electrolyte only has a minor effect on the interaction between both $FSCl_1$ and $FSCl_2$ treated surfaces (results shown in Figure 6). The fact that the surfaces are prepared by covalent modification of silica makes molecular rearrangements or desorption of the film unlikely. Previous studies[7,9,38] showed that the attractive interaction between mica hydrophobed by surfactant monolayer deposition became weaker and less long-ranged with added electrolyte, but our results indicate the opposite for silanated glass. The adhesion between $FSCl_1$ surfaces in the various salt concentrations studied increased with increased electrolyte and in 5 M NaCl the adhesion is 260 mN/m (cf. 240 mN/m in pure water). The surface tension of 5 M NaCl is γ_{lv} = 82 mN/m, and from eq 3 the calculated contact angle of 104° is the same as that calculated for pure water. Experimentally, there is also no measurable difference in the contact angle of a droplet of water and a droplet of a 5 M NaCl solution. The increase in adhesion and the agreement between the contact angles indicates that there is no change in the properties of the surfaces with increasing salt. It is also interesting to note that the long-range surface forces are about 10% stronger in 5 M NaCl than in pure water, which is about the same as the increase in liquid–vapor surface tension. Recently Craig et al.[39] have examined the effect of electrolytes on bubble coalescence in water. They found that the coalescence of air bubbles is very much reduced above NaCl concentrations of 0.1 M. Among other things they concluded that this indicated a reduction in the hydrophobic attraction; our data do not support this hypothesis.

C. Effect of Temperature. Recently results of temperature dependence on the force between two surfactant coated mica surfaces have been reported;[13] it was noted that some of the effects seen in that study could have been due to rearrangements in the monolayers on the coated surfaces.[40] The surfaces prepared by covalent modification of silica are stable and provide a good substrate for this type of study. Figure 7 shows the forces measured between $FSCl_2$ coated surfaces at room temperature and at 41 °C. There is a marked increase in the strength of the measured interaction on increasing the temperature. The size of the step also becomes larger than those present at room temperature. When the apparatus was cooled back to room temperature, the strength of the attractive interaction did not return immediately to that obtained at room temperature. After 24 h at room temperature the measured interaction was still stronger than that measured prior to heating. This is due to an extra step occurring in the force curve. If the force curve is

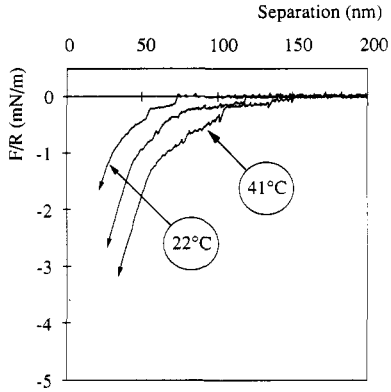

Figure 7. Forces measured between $FSCl_2$ treated surfaces as a function of temperature as indicated by the arrows. Two separate measurements are shown at room temperature and at 41 °C. The middle curve is the result at room temperature after the apparatus was allowed to cool back from 41 °C to room temperature.

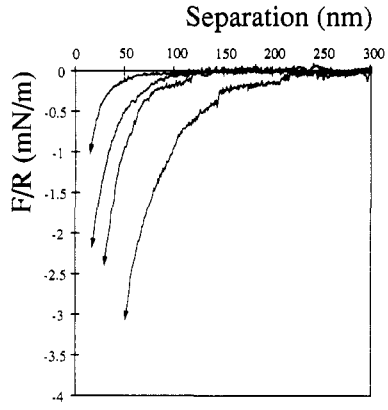

Figure 8. Forces in a 50 vol % ethanol–water mixture. The most attractive pair of curves is for pure water, and the least attractive pair is for the mixture. Each pair represents $FSCl_1$ and $FSCl_2$ coated surfaces; in both liquids the monofunctional silane is the more attractive of the two.

adjusted to remove this step, then the results after 24 h of equilibration are very close to those measured prior to heating.

D. Effect of Added Ethanol. NaCl, which increases the liquid–vapor surface tension, increases the range and strength of the attraction between hydrophobic surfaces and the adhesion between them. It was found that ethanol, which decreases the liquid–vapor surface tension, decreases the adhesion between hydrophobic surfaces and the strength of the long-range attraction between them. Figure 8 shows the forces measured in water and in 50 vol % ethanol. The force is very much reduced in range and strength compared with the measurements made in water, although the force is still very much larger than the van der Waals interaction. At 50 vol % (23 mol %) the liquid–vapor surface tension is 29.8 mN/m and the measured adhesion between $FSCl_1$ surfaces varied between 56 and 63 mN/m. This gives a calculated contact angle of between 62 and 64°. Again this value is very close to the experimentally determined contact angle. The addition of a very small amount of ethanol, <10 vol %, appears to eliminate the steps in the force curves or at least reduce their size to a point where they are immeasurable.

E. Interaction between One Hydrophobic and Hydrophilic Surface. There have been relatively few studies of the interaction between one hydrophobic and one hydrophilic surface. The first measurements concluded that the most long-range part of the force was due to an attractive double layer interaction between the surfaces whereas in order to explain the more short-range force an additional attraction had to be inferred.[41] However, more recenlty Tsao et al. used measurements in a similar system to support a dipolar electrostatic explanation for the origin of the force.[14] Measurements between a similarly charged hydrophobic surface and a bare glass surface with a very similar surface charge have been reported recently.[28] In this study no long-range attractive forces were found but instead a very short-ranged attractive interaction. Figure 9 shows the measured forces between a neutral $FSCl_1$ surface and a glass surface is 0.1 M and 1 M KBr solutions. In 1 M KBr the force curve is consistent with a van der Waals interaction (Hamaker constant (0.5–1.0) × 10^{-20} J). The normalized adhesion force in the asymmetric case was 30 mN/m.

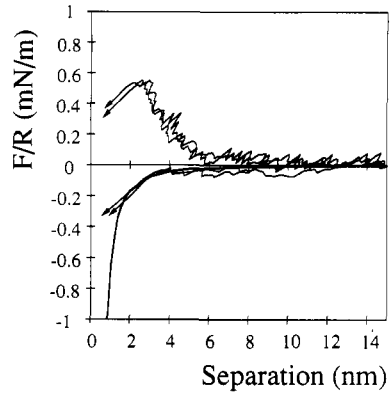

Figure 9. Forces measured between one uncharged hydrophobic surface $FSCl_1$ and one glass surface in KBr solutions of 0.1 and 1 M. The thick solid line is the calculated van der Waals interaction between two glass spheres with the plane of origin located at $D = 0$ (Hamaker constant $A = 1 \times 10^{-20}$ J). When surface deformation is taken into account according to JKR theory, the position of the undeformed surfaces is at $D = 1.3$ nm. The attractive force is with this choice of origin consistent with a van der Waals force using a Hamaker constant of 0.5×10^{-20} J.

Discussion

These measurements are carried out without the use of interferometric measurements of the surface separation. This means that any deformation of the surfaces used during the measurement will result in a change in the measured separation. When the surfaces are in adhesive contact, they will deform. This deformation is, in contrast to the deformation due to the comparatively small repulsive force experienced away from contact,[29,42] significant. The distances referred to in the figures are relative to the position of the deformed surfaces. The actual surface separation between the undeformed surfaces away from contact is smaller than indicated in the figures. The deformation for a given adhesion force can be estimated using the JKR theory.[34,35,43] The central displacement (δ) and the contact radius (a) depends on the applied force (F) and the interfacial energy (γ) as

$$a^3 = \frac{3(1-\nu^2)R}{4E}\left\{F + \frac{3\pi\gamma R}{2} + \left[\frac{6\pi\gamma RF}{2} + \left(\frac{3\pi\gamma R}{2}\right)^2\right]^{1/2}\right\} \quad (4)$$

$$\delta = \frac{2a^2}{R} - \left[\frac{4\pi\gamma a(1-\nu^2)}{E}\right]^{1/2} \quad (5)$$

where R = the radius of the spheres, E = the Young's modules, about 6×10^{10} N/m^2 for borosilicate glass,[53] and ν = the Poissons ration, about 0.2 for borosilicate glass.[53]

The interfacial energy can be calculated from the adhesion force as described above. The magnitude of the central displacement under a zero applied load calculated from eq 5 is given in Table 1. Results obtained from a more sophisticated theory indicate that these calculations may overestimate the actual surface deformation somewhat.[35] Adding the (negative) central displacement to the distances given in the figures provided a first-order correction to the data to give the force vs distance curve for undeformed surfaces.

The appearance of steps in the measured force curve provides a key piece of information in attempting to understand the origin

TABLE 1: Adhesion Forces and Surface Deformations

surfaces	solution	adhesion (mN/m)	surface displacement (nm)
silanated glass	aqueous salt solutions	240–260	−5.5
silanated glass	1:1 mixture of water and ethanol	55–65	−2.1
silanated glass vs glass	aqueous salt and solutions	30	−1.3

of the long-range attraction between hydrophobic surfaces. Since the force is the first derivative of the free energy, a discontinuity in the force implies that a separation-induced first-order phase transition occurs between the surfaces. Water between two hydrophobic surfaces is metastable to the formation of a vapor cavity, and we have seen that vapor and water can coexist at very large surface separations, eq 1. Capillary condensation is a first-order phase transition, and a discontinuity in the force has been predicted for the interaction between two surfaces in a condensing vapor[24,44] or in two immiscible liquids.[45] In these cases the force discontinuity arises from the formation of a liquid bridge between the surfaces. The analogous situation for two hydrophobic surfaces is capillary evaporation or the formation of a bridging vapor cavity between the surfaces. The experimental data indicate two distinct types of cavities, namely, microscopic or visible cavities and submicroscopic cavities.

A. Microscopic Bridging Cavities. A continuum theory for the excess free energy of cavity formation is outlined in the Appendix, and the results are plotted in Figure 10. The theory gives the free energy as a function of cavity shape for a cylindrically symmetric cavity bridging the two spherical hydrophobic surfaces. The parameters required are the pressure drop across the interface, the liquid–vapor surface energy, and the difference between the liquid–solid and the vapor–solid surface energies, which equals that of the fluid interface times the contact angle. In Figure 10 it can be seen that the optimum cavity radii decrease as the separation is increased, until about 1.5 μm beyond which there is no longer a stable or metastable minimum for these particular parameters. This is in agreement with the results of Yushchenko et al.[22]

The comparison of theory and experiment in Figure 4 gives one some confidence in the continuum theory of cavity formation, while at the same time indicating certain limitations in the approach. It is encouraging that over much of the regime the data in Figure 4a agree with the force due to the optimal bridging cavity. The fitted pressure drop of $\Delta p = -1.5 \times 10^4$ N/m^2 corresponds to an internal gas pressure of 0.85 atm, which means that the cavity contains both water vapor and other gases. Additional evidence for the nonnegligible internal gas pressure comes from the predicted and measured separations at which the cavity persists. In the case of Figure 4a, the cavity is still present at 500 nm, and in other cases, it extends out to at least 1 μm (Figure 5). A larger pressure drop would preclude any stable cavity at these separations. For example, for a pressure drop of one atmosphere, the largest stable separation is 203 nm for a contact angle of 100°, and this only increases to 625 nm for θ = 120°. Figure 10 shows that, for $\Delta p = 1 \times 10^4$ N/m^2 and θ = 100°, a cavity is stable out to about 1 μm and metastable out to 1.5 μm. This stability of the cavity at large separations is consistent with previous observations.[5] Several experiments were carried out with freshly deaerated water. In these experiments water was deaerated in a vessel and then pumped into the measuring chamber of the apparatus while a vacuum was held on the vessel. The results from these experiments and after bubbling oxygen through water were very similar, which indicates that dissolved air in the bulk water is not primarily responsible for the observation of the attraction. Note however that even a negligible amount of air dissolved in the bulk water may make a significant contribution to surface excess properties.

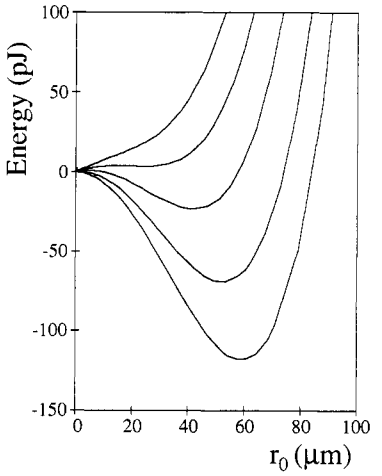

Figure 10. Free energy of cavity formation as a function of the radius of the central neck. From bottom to top the separations are h = 0.1, 0.5, 1, 1.5, and 2 μm. The parameters used are R = 2 mm, γ_{lv} = 0.072 N/m, $\Delta p = 1 \times 10^4$ N/m^2, and θ = 100°.

At very small separations and at large separations, the calculations for the microscopic bridging cavity do not agree with the experimental data. When the surfaces are in close proximity, one needs to include the direct van der Waals interaction of the solids across the vapor, as Figure 4b shows. The fact that one can describe this regime with the silica–air Hamaker constant provides additional support for the present interpretation of the data in terms of a microscopic vapor cavity. The larger separation data of Figure 4a shows a decreasing attraction from 500 to 300 nm following a change in direction from an outward to an inward run, where the cavity growth is expected to change sign from negative to positive. This is clearer in Figure 5, where four distinct regimes are evident in the hysteresis loop. The decreasing attraction just after the turn at large separations is almost certainly due to the pinning of the three-phase line on the solid surface. At some intermediate separation, the line begins to move, and the attraction slowly increases as the radius grows. Upon the reversal of direction at the smallest separation, the contact line is once more pinned, this time at the maximum radius. Finally, at some stage of the outward run movement recommences, and the contact area shrinks toward its starting value. Note that the slope of the two pinned arms is approximately parallel and shows less noise than when the three-phase line is moving. We have been able to reproduce this hysteresis loop by modeling this putative behavior in the isobaric ensemble for a bridging cylinder (not shown). The attraction decreases on the first pinned branch because the internal cavity pressure increases as the volume is decreased at a constant particle number, and the converse happens on the second pinned branch. The pinning and ocnsequent hysteresis observed here is caused by the same molecular mechanism responsible for the difference between the advancing and the receding contact angles of drops and bubbles.

B. Submicroscopic Bridging Cavities. The clear difference in the measured interaction in the presence of a microscopic cavity and the measured forces in water mean that the steps in force and subsequent attraction are not due to the formation of a microscopic bridging cavity. We now examine the possibility of submicroscopic cavities. Figure 11 shows the cavity excess free energy for small radii. In these calculations the shape of the cavity was varied to minimize the energy for each given cavity radius. The most favorable shape is such that the (macroscopic) contact angle is not achieved and there is an imbalance of the forces due to the interfacial tension at the three-phase line. Such a cavity may, however, exist provided that this imbalance can be taken up by the surface due to e.g. the presence of surface heterogeneities. It has been argued that these small cavities may exist only when there is contact angle hysteresis, as in the present case, but not

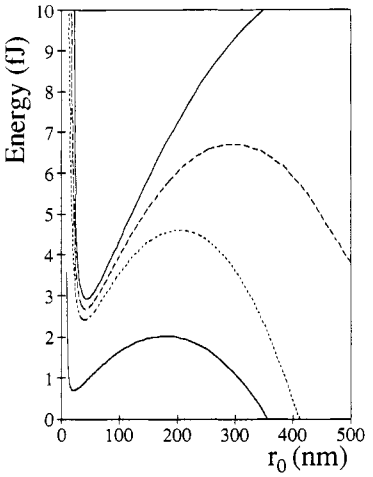

Figure 11. Metastable cavities at small radii. The solid, dashed, and dotted curves correspond to pressures of $\Delta p = -10^5$, -10^4, and $+10^5$ N/m^2, respectively, at a separation of $h = 100$ nm, and the lower solid curve corresponds to $\Delta p = -10^5$ N/m^2, $h = 50$ nm. Other parameters as in Figure 10.

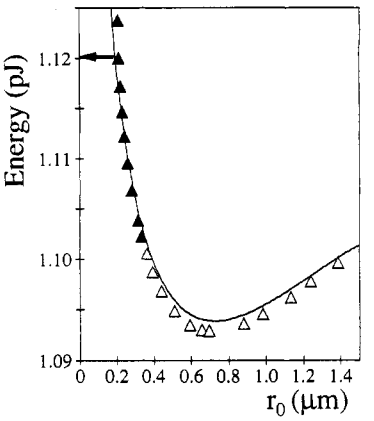

Figure 12. Gibbs free energy of the bubble of optimal shape (convex bubble shown by solid triangles; concave bubbles shown by open triangles) compared to that of a truncated hemisphere (solid curve) as a function of the radius at the mid-plane. The separation is $h = 200$ nm, and the number of particles is $Nk_BT = 2.43 \times 10^{-14}$ J. The arrow denotes the energy of the hemisphere on an isolated surface.

on perfect hydrophobic surfaces.[46] The application of the continuum model to small radii such as these can be questioned, since curvature corrections, van der Waals interactions across the neck, and fluctuations are neglected. Qualitatively, the depth of the minimum in Figure 11 decreases as the vapor pressure increases and as the separation is increased. The contact angle at this minimum is ≈150°, which is substantially larger than the macroscopic contact angle of 108°. This submicroscopic minimum originates from a change in the behavior of the shape of the cavity whereby it becomes increasingly curved as the radius of the neck is decreased. This leads to an unfavorable increase in the area of the liquid–vapor interface and a consequent increase in energy for small radii.

The submicroscopic cavities are possible candidates for the discontinuities in the measured force data. The open ensemble and the highly concave shape (with a narrow neck and the bulk of the vapor near each surface) are consistent with them being induced in the metastable liquid between the hydrophobic surfaces by a decrease in the surface separation. Figure 11 shows that they would remain stable at submicroscopic dimensions; in addition they give rise to an attractive force of similar magnitude to the observed steps (0.1–0.2 μN). Balanced against this possibility is the activation energy to their formation, and the fact that since their radius decreases with decreasing separation, the magnitude of the force also decreases; experimentally each individual step shows an increasing attraction. We are therefore motivated to explore an alternative model.

So far we have used the cavity energy derived in Appendix A, namely, the grand potential, which is appropriate for an open ensemble when diffusive equilibrium holds and the chemical potentials are everywhere the same. This model is thus appropriate for complete equilibrium. However we know that this is not experimentally obtained, as evidenced, for example, by the measured hystereiss (see Figures 4a and 5). The other limiting case which we may consider is to hold the number of vapor molecules in the cavity fixed, which is appropriate when diffusion of air into or from the cavity takes place over a longer time scale then the measurements. The isothermal–isobaric ensemble is the correct ensemble for any submicroscopic bubbles of air in the water or stuck to the surfaces. Henceforth we shall use the word "bubble" for the fixed particle number ensemble and the word "cavity" for the open ensemble. Appendix B calculates the Gibbs free energy of hemispherical bubbles. Here the neck radius of the optimal cavity was varied until its volume was consistent with the fixed number of molecules of the bubble. It was more difficult to automate the calculation, and the shape of the bubble is approximated by a hemisphere. Hence, no shape optimization is carried out for fixed number of molecules, except for Figure 12. This figure shows that the conclusions based upon these analytic results nevertheless may be relied upon, even though the actual bridging bubble is more complicated in shape. (Note that one cannot compare the energies of the grand and Gibbs ensembles because the Gibbs free energy contains an arbitrary constant; only the change in free energy in the Gibbs ensemble is meaningful.)

Figure 13a shows the force between planar surfaces due to a hemispherical bridging bubble with fixed number of molecules. The force is attractive, increasingly so at small separations, and relatively constant at large. This would correspond to a discontinuity in the force when the bubble first bridges the two surfaces. Bridging probably occurs somewhere between the coexistence separation and when the separation equals the height of the bubble on an isolated surface. The magnitude of the force obviously depends upon the initial size of the bubble, being larger when more molecules are trapped in the bubble. When the liquid–vapor surface tension is decreased, the magnitude of the constant attraction at large separations is decreased, and the critical separation for unlimited growth moves to smaller separations. This is broadly consistent with the results for ethanol, Figure 8, which reduces or eliminates the force discontinuities and which causes the final jump-in position to shift to smaller separations.

The dependence of the force on the ratio of surface energies is interesting (Figure 13b). As expected, when the hydrophobicity is increased, the magnitude of the attraction is also increased, leading to a larger initial step and a larger separation from which the surfaces will jump into contact. What is also manifest by Figure 13b is an attracive force at large separations for a bubble bridging surfaces that have a contact angle of less than 90°. In this case the magnitude of the attraction is less than for two hydrophobic surfaces, it decreases as the separation is decreased, and it eventually turns repulsive at small separations. Figure 13b shows that it is more favorable for a bubble to bridge between two surfaces than to sit on only one of them. We have not examined the asymmetric case, but nevertheless these results appear consistent with the experiments of Yoon and Yordan[47] who measured the rupture of thin water films between a microscopic bubble of air and a solid surfaces with contact angles as low as 72°. In the present picture rupture at a separation of 60 nm presumably occurs through the coalescence and subsequent growth of a submicroscopic bubble stuck to the surface. The data in Figure 9, which agree with earlier measurements[28] in showing no unusual attraction between one hydrophobic and one

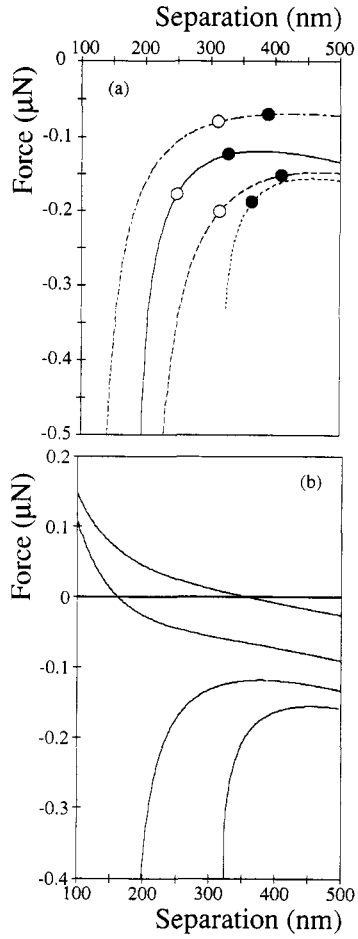

Figure 13. Force between planar surfaces due to a bridging hemispherical bubble. (a) From top to bottom, there is a dashed–dotted line (γ_{lv} = 0.036 mN/m, θ_0 = 100°, and Nk_BT = 2.43 × 10^{-14} J), a solid line (γ_{lv} = 0.072 mN/m, θ_0 = 100°, and Nk_BT = 2.43 × 10^{-14} J), a dashed line (γ_{lv} = 0.072 mN/m, θ_0 = 100°, and Nk_BT = 4.08 × 10^{-14} J), and a dotted line (γ_{lv} = 0.072 mN/m, θ_0 = 110°, and Nk_BT = 2.43 × 10^{-14} J), all in an external pressure of 1 atm. The open circles denote the height of the bubbles on the isolated surface, and the full circles denote the coexistence separation (when the free energy of the bridging bubble equals that of the bubble attached to the isolated surface). (b) From bottom to top, the curves have bulk contact angles of θ_0 = 110°, 100°, 80°, and 20°. Also, γ_{lv} = 0.072 mN/m, Nk_BT = 2.43 × 10^{-14} J, and p_0 = 10^5 N/m^2.

hydrophilic glass surface at large surface separations, can be fitted with a double layer repulsion.

When the bubble bridges the two surfaces, there results an attractive force that rapidly increases as the separation decreases and that is relatively constant and nonzero at large separations (Figure 13). The multiple steps observed in the force curves could either be due to a stepwise motion of the three-phase line along the surface or due to many bubbles bridging between the surfaces. The model force due to several bridging bubbles is compared to experimental data in Figure 14. The six bubbles were taken to be identical and situated at specific locations on the surfaces. Because the surfaces are curved (spheres, radius R = 2 mm), the local separation is greater than the separation measured on the central axis, $h(r) = h + r^2/R$, where h is the abscissa of the figures and r is the distance of the bubble from the central axis. The locations of the bubbles that were required to fit this particular force run possibly suggest that they formed around the rim of a collapsed microscopc cavity or that they result from the collapse of several long thin bridging cavities, similar to those observed between fluorocarbon surfaces.[5] The force on different runs and that measured on first approach can be expected to vary depending upon the specific arrangement of bubbles in each case. In this model the bridging was arbitrarily

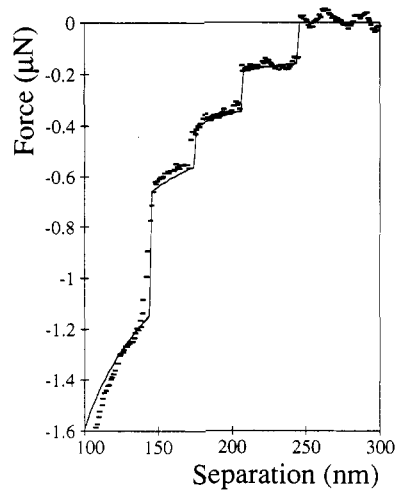

Figure 14. Measured attraction between hydrophobic $FSCl_1$ spheres (radius 2 mm) in water (symbols). The solid line represents the calculated force due to six identical hemispherical bridging bubbles (γ_{lv} = 0.072 mN/m, θ_0 = 97°, and Nk_BT = 4.37 × 10^{-14} J), one each at r = 13, 16, 18, and three at 19 μm off of the central axis, and assuming that bridging occurs when the local surface separation is $h(r)$ = 330 nm, 1 nm beyond the height of the bubble on the isolated surface.

assumed to occur when the local separation was 1 nm beyond the height of the bubble on the isolated surface. The fitted location of the bubbles is consistent with a density of 1 bubble/400 μm^2 or 0.1% surface coverage. Obviously in practice the magnitude and position of the jumps will depend upon when bridging actually occurs (i.e. the penetration beyond coexistence) and on the size and location of each bubble. The variation in the magnitude of each step in the model is due to the number of bubbles simultaneously bridging at that separation, but, in reality, a probable cause of the variation in the height of the steps is polydispersity in the bubble size and some variability and metastability in the bridging separation. One can obtain an equally good fit to the data assuming θ_0 = 100° and Nk_BT = 2.43 × 10^{-14} J and that bridging occurs at the coexistence separation, $h(r)$ = 328 nm, which is 80 nm beyond the height of these bubbles on an isolated surface. The bubbles are probably highly deformable and more responsive to the presence of the other surface than a force measuring spring, and hence bridging may possibly occur at relatively larger distances than the 1 nm beyond the undeformed height used above. At separations smaller than those shown in the figure (when the local separation is less than 190 nm), these hemispherical bublbes (and also bubbles of optimal shape) grow without limit. We have not attempted to model this dynamic process nor to include polydispersity or nonsphericity.

Given the submicroscopic bubbles are present in the bulk water, then they preferentially segregate to the surfaces and adhere to them; the energy of a bubble on the surface is much lower than a free spherical bubble because the costly liquid–vapor and liquid–solid interfaces are replaced by the less unfavorable vapor–solid contact. The submicroscopic bubbles could be attached to the surface when the surfaces are first immersed in water or they may arise in bulk solution from mechanical agitation, such as pumping or stirring, or nucleation of dissolved air around low-pressure vortexes and then attach to the surface. Although large on the molecular scale, the energy required to form submicroscopic bubbles is minute compared to typical mechanical processes. Another source of bubbles on the surfaces is the snapping of the microscopic cavity bridge that has formed after the surfaces have been separated from contact.[5] This vapor has to go somewhere, and it seems more likely that the cavity will break up into tiny bubbles than that it will dissolve immediatley in the water. This is particulalry true if it consists mainly of air, as was argued above; because of its decreased internal pressure it acts as a localized de-aerator. Force measurements are typically made

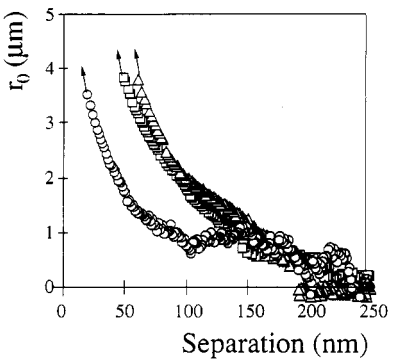

Figure 15. Mid-plane radius of a bridging bubble or cavity that would give the measured force at small separations for $FSCl_1$ treated surfaces in water (squares, γ_{lv} = 72 mN/m), in 5 M NaCl (triangles, γ_{lv} = 82 mN/m), and in 50% ethanol (circles, γ_{lv} = 29.8 mN/m). See text for details.

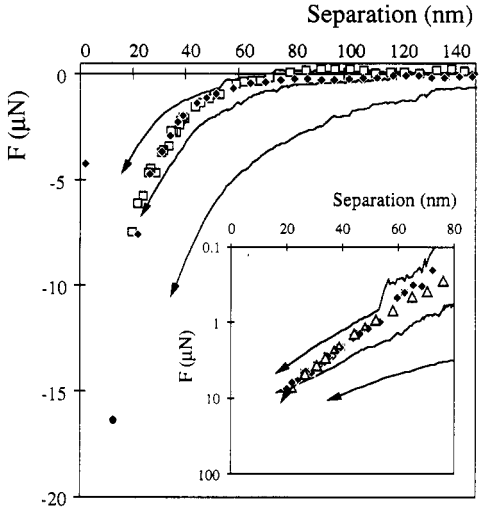

Figure 16. Actual force between hydrophobic spheres (radius 2 mm) in water (solid lines) for $FSCl_2$ treated surfaces (least attractive two solid lines) and $FSCl_1$ treated surfaces (strongest attraction) compared with the force measured between DDOABr coated surfaces (symbols).

after initial contact of the surfaces to establish the zero of separation, and for highly hydrophobic surfaces each force curve generates a visible microscopic cavity. However, the forces observed on first contact between hydrophobed mica are long-ranged, and similarly measurements of the forces on first contact between the glass surfaces were also long-ranged.

Bubbles, whether in bulk or attached to surfaces, are thermodynamically unstable. Given sufficient time, the air will dissolve in the water and return to the atmosphere. However this may be a comparatively slow process, and bubbles may be generated at a faster rate than they dissolve. Hence it is arguable that the isobaric ensemble (constant particle number, fluctuating volume) is the most appropriate one and that mechanical rather than diffusive equilibrium holds during the course of an experiment. If the internal pressure should fall below the vapor pressure of water, then the grand ensemble probably applies. The size and density of attached bubbles is probably dependent upon the nature of each specific hydrophobic surface and the details of the experimental procedure such as the filling of the apparatus with water and mixing of the solution. Hence, the force may be expected to vary between different experiments. This may explain the large discrepancy in range and magnitude of the attraction reported for different hydrophobic surfaces with rather similar macroscopic contact angles (2–14°). We note that for surfaces with contact angles above 100° the range of the attractive force reported in water vary between 300 nm[10] to no longer than expected for a van der Waals force.[48,49] The increase in range of the attraction with increased temperature (Figure 7) may be due to a growth in size of the bubbles as air de-dissolves from the water and as the surface tension decreases.

At separations smaller than shown in Figure 14 there is no stable submicroscopic minimum in the isobaric ensemble. The bubbles or cavities grow without bound, and the force is some nonequilibrium result of the dynamics of the growth process as the surfaces jump into contact. From the equation for mechanical balance across the midplane, $F = \pi r_0^2 \Delta p - 2\pi r_0 \gamma_{lv}$, an estimate can be made of the size of the bridging cavity or bubble at smaller separations, $r_0 = -(\gamma_{lv}/\Delta p)(-1 + [1 + \Delta p F/\pi\gamma_{lv}^2]^{1/2})$. Since true equilibrium does not hold (the cavity is either pinned or in the process of growing), it is emphasized that this is no more than a crude guide to the size of the cavity that would give the measured forces. The results are shown in Figure 15 using the known surface tensions, a pressure drop of 1 atm, and the measured force as a function of separation. In general the size of the bridge grows as the separation decreases and is of the order of microns in radius for all three liquids. It is larger in 5 M electrolyte and smaller in the ethanol–water mixture. There are possibly two regimes: a slowly increasing and more noisy regime at large separations, and a smooth steadily increasing small-separation regime. By contact the cavity is approaching the size of the microscopic cavities that become visible when the surfaces are separated. We note that the predicted size of the bubble is such that it ought to be just possible to see it with the interferometric surface force technique. Nevertheless, no paper describing the appearance of a vapor cavity before surface contact has been presented. Hence, if a bubble is present between the hydrophobed mica surfaces and gives rise to the hydrophobic force also in that case, they have to be of smaller size than this crude prediction.

C. Validity of The Derjaguin Approximation. The agreement between the measurements and the theory for submicroscopic bridging bubbles/cavities gives us some considerable confidence that the force data obtained here is primarily due to bubbles bridging the surfaces. However the relevance of these observations to the measurements between hydrophobic surfaces in the interferometric surface force apparatus (SFA) is not immediately apparent. First there is no report of the observation of force discontinuities in those studies, and second the magnitude of the interaction free energy (F/R) is considerably smaller in the earlier work. One might well argue that the forces in the mica system are the true "hydrophobic interaction" and that this is being masked by the presence of the bubbles in this study. It cannot be ruled out that what today is called "the hydrophobic interaction between macroscopic surfaces" indeed is due to several different mechanisms. For instance, there is nothing strange with the strong adhesion force which simply is a consequence of the high interfacial tension against the aqueous phase. However, we argue that the most long-range part of the force in all cases could be due to the presence of submicroscopic cavities/bubbles. Concerning the magnitude of the force, bridging bubbles or cavities do not obey the Derjaguin approximation, which relates the force scaled by the radius of curvature to the interaction free energy. The force is due to the contact of a bubble with an opposing surface, so the radius of the surface only determines the number of bubbles that are within a particular distance from the opposing surface and not the magnitude of the force (cf. the present calculations for hemispherical bubbles, which were for planar surfaces). At the extremely low densities of bubbles on the surface needed to produce the force, then it is likely that only one or two bridging bubbles/cavities are normally involved in the interaction. As a result the actual force is largely independent of the radius of curvature of the surfaces (obviously when the radius of curvature is very small, this will affect the size and shape of the bubble). Figure 16 shows a comparison of the actual forces between DDOABr coated mica surfaces and the measurements obtained in this study. This is in contrast to the "traditional" presentation of Figure 1, where the force is scaled by the respective radii, implicitly assuming the

applicability of the Derjaguin approximation. The similarity between the DODABr results and the $FSCl_2$ results which have similar surface energies is quite remarkable. The $FSCl_1$ results are considerably stronger; however, there are multiple steps present in this data and the receding contact angle is considerably higher than the DODABr surface, so more bubbles and a stronger interaction are expected. We note that this is probably the only measured surface force which does not obey the Derjaguin approximation, which in itself may be taken as additional support for the mechanism proposed here.

D. Comparison with Observations of Cavitation. Another major difference between these results and those obtained for hydrophobed mica is the observation of the steps in the force curve. The fact that no steps are reported in the forces between hydrophobized mica surfaces does not necessarily indicate that the forces observed in these systems are not due to the bubble bridging mechanism discussed here. Attractive forces can be measured with the interferometric SFA in two different ways. The most accurate is the dynamic method in which the surfaces are driven together at constant speed and the separation is determined from video recordings of the fringes, and the number of data points which can be collected for a force run is at best a few hundred. As a result it would be difficult to see the small changes in separation resulting from a step. The force resolution for the bimorph-based surface force apparatus is higher than for the interferometric-based apparatus, and many thousands of points can be collected. The size of the steps is less than 0.2 μN, which is close to the resolution of the interferometric SFA. Furthermore, the radius of curvature of the surfaces used in the mica experiments is 10 times larger than the glass surfaces used in the present study. The hydrodynamic force as a result would be 100 times larger, and this would slow the motion of the surfaces when an abrupt change in force due to a step is encountered making the step less noticeable if present. The spring jump method can also be used to measure attractive forces with the SFA. The position at which the surfaces jump into contact is recorded as a function of the spring constant and the derivative of the force is measured. The observation of steps would be extremely difficult with this technique. Finally the addition of ethanol wipes out the appearance of the steps in forces between hydrophobized glass. The steps are rather sensitive to the specific hydrophobic surface (cf. $FSCl_1$ and $FSCl_2$, Figures 6 and 8) and the surface tension of the liquid.

The observations of the behavior of the microscopic cavity in the hydrophobed glass system are similar to the observations of the behavior of cavities in the mica system. Cavities were found to be stable out to separations of 0.5–1 μm for hydrocarbon coated mica surfaces, which is too large a separation for a cavity to exist if it were comprised only of water vapor. This leads to the conclusion that some air is contained in these cavities also. For fluorocarbon coated mica surfaces the cavities are stable out to very large surface separations (many microns), and it was noted in these experiments that the size of the cavity would increase with time as the experiment progressed presumably due to the dissolution of air into the water. The most intringuing observation in these experiments was the way the cavities formed around the contact region for fluorocarbon surfactant coated mica. In the mica experiments cavitation was not observed prior to surface contact.[5] For fluorocarbon coated surfaces numerous small cavities with radii $\approx$ 1–10 μm formed around the perimeter of the contact zone.[5] These small cavities are relatively stable, and as the surfaces are separated, they move around and coalesce to form one large cavity. The multiple steps present in the force curves recorded between silanated glass surfaces are certainly the result of the same multiple cavity or bridging bubble formation. Perhaps the only difference being that for the hydrophobed glass system, this is observed *prior* to the surfaces contacting.

E. Nonaqueous Solvents. There has been only one study of the interaction between hydrophobic mica surfaces in nonaqueous solvents. The forces between mica surfaces coated with a fluorocarbon surfactant were measured in ethylene glycol and its mixtures with water.[11] The surfaces in this studied had a high contact angle, $\sim$94° advancing, with a drop of pure ethylene glycol as test liquid. The force in pure ethylene glycol had a range and strength similar to the van der Waals attraction, and when the surfaces contacted, cavitation was observed. Increasing the water content from 0 to 50 vol % causes the strength and the range of the force to increase to that found in pure water. This is qualitatively in agreement with the measurements of the forces made between $FSCl_1$ and $FSCl_2$ treated glass surfaces in water and mixtures of ethanol; i.e., a decrease in liquid vapor surface tension results in a reduction of the strength and range of the range of the attractive interaction. Ethylene glycol has a liqiud–vapor surface tension γ_{lv} = 47.7 mN/m, which is higher than the surface tension of a 50% ethanol water mixture. On the basis of this alone a long-range force may have been expected in pure ethylene glycol. The fact that this was not observed in the SFA experiments may be due to other factors such as the solubility of gas, the viscosity, or even the order of dilution. It is possible that bubbles which are metastable persist to low liquid–vapor surface tensions when water is diluted with an additive. However, the surface forces may be quite different if the order is reversed, i.e. starting with pure ethanol or pure ethylene glycol and diluting with water. We are currently testing this hypothesis and will report the results in a forthcoming publication.

F. Comparison with AFM Measurements. Very recently there have been a number of measurements of the hydrophobic interaction between very small particle/tips and a surface with the atomic force microscope. Tsao et al.[38] reported measurements of the force between a hydrophobed silica nitride atomic force microscope tip and a hydrophobic monolayer on mica. They concluced that their measuremnets were of the same range and strength as the measurements made in the SFA. This was based on the use of the Derjaguin approximation applied to a pyramidal tip. The radius of a standard silicon nitride atomic force microscope tip has been found to be of the order of 100 nm,[50] i.e. the same as the length scale of the interaction. Quantitative comparison with this data depends critically on the tip shape. If we assume, as others, that the tip shape is spherical, then the range and strength of the interaction measured between the hydrophobed tip and hydrophobed mica surface deduced from the Derjaguin approximation are considerably less than those measured between larger radii surfaces. The radii of the tips are smaller than the size of the bubbles required to explain the data we present. This will certainly influence the size of the bubble and reduce the interaction or maybe no bubble is present between the tip and surface in the AFM experiments.

In another study the interaction between a hydrophobic colloid (polystyrene coated AFM tip) and a hydrophobic surface (polystyrene plate) was measured with an AFM.[51] It was found that in pure water the surfaces jumped into contact from a larger separation (20–30 nm) than expected from van der Waals theory (5 nm). The jump in these experiments occurred at a larger separation than the observation of the onset of the attraction (5–10 nm) reported by Tsao et al.[38] The attraction was not measured in these experiments only the jump position; i.e. the force between the probe and the surface remained at zero until the surfaces jumped into contact. It is possible that the jump observed in these experiments is due to a step appearing in the force curve. Very weak spring constants are used in these experiments, so data at smaller separations are inaccessible due to the spring instability.

Conclusion

The experimental data presented here appear to rule out two previous explanations for the long-ranged attractions between

hydrophobic surfaces. First, mechanisms that invoke electrostatics to account for the range of the force[14,16,17] are contradicted by the insensitivity to electrolyte found here and previously,[9] even though such mechanisms were plausible when considering some early data (7, 13–14). Second, the long-ranged attractions that occur upon approach to a separation-induced spinodal[19] although formally exact, do not appear applicable to the hydrophobic attraction because the force discontinuities in the present data indicate that the phase transition occurs prior to the appearance of the long-range force and not the other way around. In addition, the correlation length of bulk water does not become of the order of 10 nm (approximately the decay length of the hydrophobic attraction), until one is almost at the bulk spinodal, where the density would be reduced by about 20% from its bulk value.[52] The consequent reduction in the refractive index would probably be observable experimentally if the theory were applicable to the long-ranged attractions between hydrophobic surfaces.

It is suggested here that the long-ranged attraction between hydrophobic surfaces is due to bridging of submicroscopic bubbles. The discontinuities in the force at the large-separation onset of the attraction appear to be due to the consecutive bridging of bubbles present on the surfaces. We showed that the data could be quantitatively described by a model with very low surface coverage of bubbles and suggested that the bubbles arise from mechanical agitation or from the collapse of the microscopic cavity that forms after contact. We argued that since electrolyte does not measurably increase the surface tension of water until about 1 M, the observed insensitivity to salt concentration of the hydrophobic attraction was consistent with the mechanism of bridging bubbles. We also suggested that the increase in range of the attraction with increased temperature is due to a growth in size of the bubbles as air dedissolved from the water; the fact that the attraction did not decrease completely to its original form at room temperature was probably due to a single extra bridging bubble between the surfaces. The lack of steps in ethanol was argued as being related to the decrease in the liquid–vapor surface tension.

The strongest argument for bridging bubbles or cavities as the origin of the measured long-range attraction between hydrophobic surfaces is the quantitative agreement between theory and experiment, Figure 14. Although one has a certain freedom in choosing the number, size, and location of the bubbles, the consequent force is determined unambiguously by the continuum model, and it is this invariable qualitative behavior that makes the quantitative fit to the data possible. One can state that *if* these bubbles were present, *then* this is the force that would be measured. More general statements are precluded by the dependence of the predicted forces on the specific arrangement of bubbles, and indeed any series of measurements show a similar variability. Further, the most realistic model of the experimental situation likely lies somewhere between the cavities of the grand ensemble (full equilibrium) and the bubbles of the isobaric ensemble (restricted diffusion) used here. Nevertheless, bridging bubbles explain the experimental data presented here. They represent a physical connection between the two surfaces at large separations, and hence they avoid the difficulty of reconciling the measured range of the interaction with fundamental notions of the structure of liquids and the influence of surfaces. It is possible to rationalize a number of earlier observations and measurements on the basis of this model, although the presence of bridging bubbles in the SFA data remains to be proved or disproved. Hence, one may explain all data as originating from bridging bubbles/cavities, or we have to accept that more than one mechanism for the long-range part of the so called hydrophobic interaction is at play.

Acknowledgment. We would like to thank Jan Christer Eriksson and Stig Ljunggren for critically reading the manuscript and for many stimulating and invaluable discussions. J.L.P. and P.M.C. acknowledge financial support from the Swedish Natural Science Research Council (NFR).

Appendix A. Energy of Cavity Formation

This appendix is concerned with the continuum theory for the free energy of a bridging cavity. The calculation is based upon the Eular–Lagrange optimization of the cavity energy with respect to shape, which is equivalent to an earlier approach using the Laplace–Young equation.[22] The energy may be divided into two contributions, $E_T = E_v + E_s$. The vapor energy, of the cavity E_v is

$$E_v = -\Delta p V_v + \gamma_{lv} A_v \tag{A1}$$

where $\Delta p = p_v - p_l$ is the pressure drop, $\gamma_{lv} > 0$ is the liquid-vapor surface energy, V_v is the volume of the cavity, and A_v is the area of the fluid interface. The second term is the energy of the solid surface,

$$E_s = \Delta\gamma A_s \tag{A2}$$

where $\Delta\gamma = \gamma_{sv} - \gamma_{sl} = \gamma_{lv} \cos\theta_0$ is the difference in surface energies, which is related to the bulk contact angle, and A_s is the area of the cavity in contact with the solid surface. $\Delta p < 0$, and the vapor energy is positive, making it unfavorable to form the cavity. For hydrophobic surfaces $\Delta\gamma < 0$, the solid energy is negative, driving the formation of the cavity. These expressions represent the grand potential of the cavity, which is appropriate when the vapor/gas of the cavity is in diffusive equilibrium with the water and the atmosphere; both the chemical potential and the pressure drop are constant in this case. Mechanical equilibrium may be expected to be established much more quickly than diffusive equilibrium, and in some cases the time scales of the latter may be longer than the experimental times. In these circumstances it is more appropriate to use the Gibbs free energy for the isothermal–isobaric ensemble (constant particle number, fluctuating volume), as is done for the case of hemispherical bubbles in the following appendix.

The cavity energy is a function of the shape of the cavity. We use a cylindrical coordinate system with the z-axis connecting the two identical solid surfaces and the radial coordinate perpendicular to the central axis. The cavity surface is described by the function $z(r)$, which is parametrized by the radius at the midplane, r_0. This is either the minimum or the maximum radius, depending on whether the cavity is concave or convex, respectively. The cavity intersects the solid surface at (r_s,z_s), and again r_s is an extremum. For identical convex bodies of separation h (measured along the central axis between the points of closet approach), $z_s \geq h/2$. The area of the cavity is

$$A_v = 4\pi \int_{r_0}^{r_s} [1 + \dot{z}(r)^2]^{1/2} r \, dr \tag{A3}$$

and its volume is

$$V_v = 2\pi \int_{r_0}^{r_s} \dot{z}(r) r^2 \, dr - V_s \tag{A4}$$

where $\dot{z}(r) = dz/dr$ and V_s is the volume of the solid included in the cavity integral (see below). The vapor energy is a functional of the cavity shape $E_v\{z(r)\}$, and it may be minimized by the standard Euler–Lagrange equations. The result is

$$\dot{z}(r) = \frac{\pm|(1+q)r_0^2 - r^2|}{[(r^2 - r_0^2)((1+q)^2 r_0^2 - r^2)]^{1/2}}, \quad q \equiv \frac{-2\gamma_{lv}}{\Delta p r_0} \tag{A5}$$

The boundary conditions at the symmetry plane are $z(r_0) = 0$, $\dot{z}(r_0) = \infty$. It proved convenient to evalulate numerically this profile equation directly, rather than to express it in terms of

elliptic integrals. The sign of the derivative determines whether the cavity is concave or convex, and there are four regimes:

$$q > 0, \quad 1 < r/r_0 < [1 + q]^{1/2} \tag{A6a}$$

$$-1 < q < 0, \quad 1 > r/r_0 > [1 + q]^{1/2} \tag{A6b}$$

$$-2 < q < -1, \quad 1 > r/r_0 > -(1 + q) \tag{A6c}$$

$$q < -2, \quad 1 < r/r_0 < -(1 + q) \tag{A6d}$$

Convex cavities have $r < r_0$, and concave ones have $r > r_0$. The case of $q = -1$ corresponds to a hemisphere of radius r_0. Negative pressure drops ($q > 0$) yield concave or saddle-shaped cavities. One can also have a concave cavity for a small r_0 or a small excess internal pressure (q large and negative).

For two convex solid bodies characterized by mutual radius S large compared to the separation, the local separation is

$$h(r) = h + \frac{r^2}{2S} \tag{A7}$$

the area of the solid–vapor interface is

$$A_s = 2\pi r_s^2\left(1 + \frac{r_s^2}{4S^2}\right) \tag{A8}$$

and the volume removed from the cavity by the solid is

$$V_s = \frac{\pi r_s^4}{4S} \tag{A9}$$

Another quantity of interest is the angle of contact at the three-phase line, and this is

$$\cos\theta = -\frac{1 + r_s\dot{z}(r_s)/S - r_s^2/2S^2}{[1 + \dot{z}(r_s)^2]^{1/2}} \tag{A10}$$

These expansions are valid when $r/S \ll 1$. In actual fact, for the case treated in the text (two spheres each of radius R, $S = R/2$) we used the exact expressions

$$h(r) = h + 2(R - [R^2 - r^2]^{1/2}) \tag{A11}$$

$$A_s = 4\pi R(R - [R^2 - r_s^2]^{1/2}) \tag{A12}$$

$$V_s = \frac{2\pi}{3}(2R^3 - 3R^2(R^2 - r_s^2)^{1/2} + (R^2 - r_s^2)^{3/2}) \tag{A13}$$

$$\cos\theta = -\frac{r_s\dot{z}(r_s) + [R^2 - r_s^2]^{1/2}}{r[1 + \dot{z}(r_s)^2]^{1/2}} \tag{A14}$$

The solution of the Eular–Lagrange result, eq A5, gives the profile that minimizes the vapor energy for a given r_0, and consequently the total cavity energy may be found as a function of the midplane radius. Cavities corresponding to certain values of q and r_0 that do not bridge the two surfaces at a particular separation are discarded. For bridging cavities, the equilibrium size and shape are of minimum energy. We find numerically that at this minimum in the total energy, the contact angle at the surface equals the bulk contact angle $\cos\theta = \cos\theta_0$. (In our procedure we specify the difference in solid surface energies, which is determined from the bulk contact angle, but allow the cavity to have any contact angle at the surface.) Instead of actually minimizing the energy, Yushchenko et al.[22] imposed the bulk contact angle as a boundary condition. The two approaches should agree at the global minimum although we have not been able to derive a mathematical proof that the energy is minimized by the bulk contact angle. Ljunggren and Eriksson have subsequently given a mathematical proof that an extremum of the grand potential occurs at the bulk contact angle.[46] In general the force acting on the surfaces is the derivative of the total energy with separation $F = -dE_T/dh = -\partial E_T/\partial h - \partial E_T/\partial r_s\,(dr_s/dh)$. For the optimal cavity the last term vanishes and the remaining term may be expressed as the mechanical balance across the midplane, $F = \pi r_0^2\Delta p - 2\pi r_0\gamma_{lv}$.

In addition to the global minimum just discussed, we found a local minimum in the energy at small radii, $\partial E_T/\partial r_0 = 0$. Here the contact angle is much greater than the bulk contact angle, and the cavities are extremely convex. For this minimum the radius at the surface was at its smallest, $\partial r_s/\partial r_0 = 0$, and the energy increased as a function of r_s, $\partial E_T/\partial r_s > 0$. This small radius local minimum was missed by Yushchenko et al.[22] At this minimum the force between the surfaces is not given by the midplane mechanical balance; we evalulate it by numerical derivative of the free energy.

Appendix B. Energy of Bubble Formation

This appendix is concerned with the energy of hemispherical bubbles as a function of size at constant particle number. The pressure inside a bubble is greater than that in the surrounding liquid. We shall suppose that each bubble is comprised of a fixed number of air molecules, assuming that mechanical rather than diffusive equilibrium holds due to the short duration of the measurements and to the limited amount of air dissolved in the water. This is in contrast to the previous appendix, where we assumed that the cavities were comprised mainly of water vapor at the same chemical potential as the surrounding liquid. We shall also restrict our attention to hemispherical bubbles rather than finding the optimum shape. This allows analytic results to be obtained and may be viewed as an expansion valid for $q \approx -1$. We consider the vapor to be ideal, and the Gibbs free energy is

$$G = p_0V - Nk_BT\ln V + \gamma_{lv}A + \Delta\gamma A_s \tag{B1}$$

where p_0 is the pressure of the liquid, N is the number of molecules of the vapor, k_BT is the thermal energy, and $\Delta\gamma = \gamma_{sv} - \gamma_{sl}$. In this expression an arbitrary constant has been neglected (cf. the argument of the logarithm), so it is only useful for comparing changes in Gibbs free energy, not absolute values.

For a free spherical bubble in the bulk liquid and of radius R, the volume is $V = 4\pi R^3/3$, the surface area is $A = 4\pi R^2$ and $A_s = 0$. The equilibrium radius minimizes the Gibbs free energy, and one obtains the familiar Laplace–Young equation,

$$R = 2\gamma_{lv}/\Delta p \tag{B2}$$

where $\Delta p = p_v - p_0$, $p_v = Nk_BT/V(R)$, and $\partial^2G/\partial R^2 > 0$. A bubble in contact with one surface assumes a hemispherical shape of radius R and contact angle θ_{svl}. With $t = \cos\theta_{svl}$, one has

$$V = \frac{\pi R^3}{3}(2 - 3t + t^3) \tag{B3}$$

$$A = 2\pi R^2(1 - t) \tag{B4}$$

$$A_s = \pi R^2(1 - t^2) \tag{B5}$$

One finds that the Gibbs free energy is minimized by

$$\Delta\gamma = -\gamma_{lv}\cos\theta_{svl} \tag{B6}$$

which is just Young's equation (the contact angle of a water drop

is $\theta_{slv} = \theta_0 = \pi - \theta_{svl}$), and

$$R = 2\gamma_{lv}/\Delta p \tag{B7}$$

with $p_v = Nk_BT/V(R,t)$.

For a hemispherical drop of radius R symmetrically confined between two planar surfaces separated by h one has

$$V = \pi R^2 h - \pi h^3/12 \tag{B8}$$

$$A = 2\pi Rh \tag{B9}$$

$$A_s = 2\pi(R^2 - h^2/4) \tag{B10}$$

It is emphasized that the curvature of the solid surfaces has been ignored in these expressions since we expect to apply them only for submicroscopic sizes. One finds for the hemispherically shaped bubble (which is not the true equilibrium shape) that $(\partial G/\partial R)_{N,T,h} = 0$ when

$$R = \frac{-\gamma_{lv}h}{2\Delta\gamma - \Delta ph} \tag{B11}$$

where $p_v = Nk_BT/V(R,h)$. This extremum is a minimum at larger separations. At small separations ($h \lesssim -2\Delta\gamma/p_0$) the solid surface energy dominates, and there is no stable hemispherical bubble. The contact angle is given by $\cos\theta_{svl} = -h/2R$. For this shape of the bubble neither the Laplace–Young nor the Young equation is satisfied by this expression except when $\Delta\gamma = \gamma_{lv}$, $h = 2R$ (they would be satisfied for the optimum shape). The reason is that for fixed separation, the single parameter R of the hemispherical bubble is insufficient to simultaneously optimize the free energy with respect to volume, surface area, and contact area, and eq B11 represents the best compromise. The net force between surfaces bridged by a hemispherical bubble where ΔP and the number of particles is independent of h is

$$F = \Delta p(\pi R^2 - \pi h^2/4) - 2\pi R\gamma_{lv} + \pi\Delta\gamma h \tag{B12}$$

References and Notes

(1) Israelachvili, J. N.; Pashley, R. M. *J. Colloid Interface Sci.* **1984**, *98*, 500–514.
(2) Pashley, R. M.; McGuiggan, P. M.; Ninham, B. W.; Evans, D. F. *Science* **1985**, *229*, 1088–1089.
(3) Claesson, P. M.; Blom, C. E.; Herder, P. C.; Ninham, B. W. *J. Colloid Interface Sci.* **1986**, *114*, 234–242.
(4) Claesson, P. M.; Christenson, H. K. *J. Phys. Chem.* **1988**, *92*, 1650–1655.
(5) Christenson, H. K.; Claesson, P. M. *Science* **1988**, *239*, 390–392.
(6) Rabinovich, Y. I.; Derjaguin, B. V. *Colloids Surf.* **1988**, *30*, 243–251.
(7) Christenson, H. K.; Claesson, P. M.; Berg, J.; Herder, P. C. *J. Phys. Chem.* **1989**, *93*, 1472–1478.
(8) Parker, J. L.; Cho, D. L.; Claesson, P. M. *J. Phys. Chem.* **1989**, *93*, 6121–6125.
(9) Christenson, H. K.; Fang, J.; Ninham, B. W.; Parker, J. L. *J. Phys. Chem.* **1990**, *94*, 8004–8006.
(10) Kurihara, K.; Kato, S.; Kunitake, T. *Chem. Lett.* **1990**, *9*, 1555–1558.
(11) Parker, J. L.; Claesson, P. M. *Langmuir* **1992**, *8*, 757.
(12) Christenson, H. K.; Claesson, P. M.; Parker, J. L. *J. Phys. Chem.* **1992**, *96*, 6725.
(13) Tsao, Y.; Yang, S. X.; Evans, D. F.; Wennerström, H. *Langmuir* **1991**, *7*, 3154.
(14) Tsao, Y. H.; Evans, D. F.; Wennerström, H. *Langmuir* **1993**, *9*, 779.
(15) Eriksson, J. C.; Ljunggren, S.; Claesson, P. M. *J. Chem. Soc., Faraday Trans. 2* **1989**, *85*, 163.
(16) Attard, P. *J. Phys. Chem.* **1989**, *93*, 6441.
(17) Podgornik, R. *J. Phys. Chem.* **1989**, *92*, 5840.
(18) Ruckenstein, E.; Churaev, N. *J. Colloid Interface Sci.* **1991**, *147*, 535.
(19) Bérard, D. R; Attard, P.; Patey, G. N. *J. Chem. Phys.* **1993**, *98*, 7236.
(20) Attard, P.; Ursenbach, C. P.; Patey, G. N. *Phys. Rev. A* **1993**, *45*, 7621.
(21) Yaminsky, V. V.; Yushchenko, V. S.; Amelin, E. A.; Shchukin, E. D. *J. Colloid Interface Sci.* **1983**, *96*, 301.
(22) Yushchenko, V. S.; Yaminsky, V. V.; Shchukin, E. D. *J. Colloid Interface Sci.* **1983**, *96*, 307.
(23) Gregg, S. J.; Sing, K. S. W. *Adsorption Surface Area and Porosity*; Academic Press: New York, 1982.
(24) Evans, R. *J. Phys.: Condens. Matter* **1990**, *2*, 8989.
(25) Sarman, S.; Eriksson, J. C.; Kjellander, R.; Ljunggren, S. *Progr. Colloid Polym. Sci.* **1987**, *74*, 76.
(26) Parker, J. L.; Yaminsky, V.; Claesson, P. M. *J. Phys. Chem.* **1993**, *97*, 7706.
(27) Parker, J. L.; Rutland, M. W. *Langmuir* **1993**, *9*, 1965.
(28) Parker, J. L.; Claesson, P. M. *Langmuir* **1994**, *10*, 635.
(29) Parker, J. L. Manuscript in preparation.
(30) Tripp, C. P.; Hair, M. L. *Langmuir* **1991**, *7*, 923.
(31) Tripp, C. P.; Hair, M. L. *J. Phys. Chem.* **1993**, *97*, 5693.
(32) Parker, J.; Claesson, P. M.; Erlandson, R. Manuscript in preparation.
(33) Israelachvili, J. N. *Intermolecular and Surface Forces*, 2nd ed.; Academic Press: London, 1991.
(34) Johnson, K. L.; Kendall, K.; Roberts, A. D. *Proc. R. Soc. London Ser. A* **1971**, *324*, 301.
(35) Attard, P.; Parker, J. L. *Phys. Rev. A* **1992**, *46*, 7959–7971.
(36) Hertz, H. *J. Reine Angew. Math* **1881**, *92*, 156.
(37) Christenson, H. K. *J. Colloid Interface Sci.* **1988**, *121*, 170–178.
(38) Tsao, Y. H.; Evans, D. F.; Wennerström, H. *Sciences* **1993**, *262*, 547.
(39) Craig, V. S.; Ninham, B. W.; Pashely, R. M. *J. Phys. Chem.* **1993**, *97*, 10192.
(40) Christenson, H. K.; Parker, J. L.; Yaminsky, V. *Langmuir* **1992**, *8*, 2080.
(41) Claesson, P. M.; Herder, P. C.; Blom, C. E.; Ninham, B. W. *J. Colloid Interface Sci.* **1987**, *118*, 68–79.
(42) Parker, J.; Attard, P. *J. Phys. Chem.* **1992**, *96*, 10398–10405.
(43) Horn, R. G.; Israelachvili, J. N.; Pribac, F. *J. Colloid. Interface Sci.* **1987**, *115*, 480–492.
(44) Balbuena, P. B.; Berry, D.; Gubbins, K. E. *J. Chem. Phys.* **1993**, *98*, 638.
(45) Forcada, M. L. *J. Chem. Phys.* **1993**, *98*, 638.
(46) Eriksson, J. C.; Ljunggren, S. Personal communication.
(47) Yoon, R. H.; Yordan, J. *J. Colloid Interface Sci.* **1991**, *146*, 565.
(48) Parker, J. L.; Claesson, P. M.; Wang, J. H.; Yasuda, H. K. *Langmuir*, in press.
(49) Woods, J.; Sharma, R. Manuscript in preparation.
(50) Hutter, J. L.; Bechhoefer, J. *Rev. Sci. Instrum.* **1993**, *64*, 1868.
(51) Karaman, M. E.; Meagher, L.; Pashley, R. M. *Langmuir* **1993**, *9*, 1220.
(52) Attard, P. Unpublished calculations.
(53) *Kirk Othmer Encyclopedia of Chemical Technology*; Wiley: New York, 1980; Vol. 11, p 830.